



Cite this: *Chem. Commun.*, 2020, 56, 450

Received 22nd November 2019,  
Accepted 29th November 2019

DOI: 10.1039/c9cc09092d

[rsc.li/chemcomm](http://rsc.li/chemcomm)

**Integration of the material preparation step into the device fabrication process is of prime importance for the development of high performance devices. This study presents an innovative strategy for the *in situ* assembly of graphene-based aerogels on a chip by polymerization-reduction and annealing processes, which are applied as chemiresistive gas sensors for the detection of NO<sub>2</sub>.**

Graphene aerogels represent an emerging category of porous conductive materials with hierarchical pore structures and high specific surface area, which have received enormous interest in energy storage and conversion,<sup>1</sup> environmental remediation,<sup>2</sup> catalysis<sup>3</sup> and gas sensors.<sup>4</sup> The adsorption of gas molecules on graphene's surface leads to changes in its electrical conductivity that can be attributed to the change in the local charge carrier density induced by the surface adsorbates which act as electron donors or acceptors.<sup>5</sup> Besides the adsorption onto low-energy binding sites ( $sp^2$ -bonded carbon), that onto higher-energy binding sites such as vacancies, defects, and functional groups on the surface of graphene leads to an improved change in the conductance of graphene-based sensors.<sup>6</sup> Furthermore, assembly of 2D graphene sheets into 3D hydrogel/aerogel structures is a promising way for enhancing sensing performance by maintaining a high surface area in an accessible porous network.<sup>7</sup> Up to now, most efforts have been ongoing to focus on chemical modifications<sup>7c,8</sup> and functionalization of graphene-based aerogels, such as those decorated with metal oxides and transition metal sulphides.<sup>7b,9</sup>

However, up to now the fabrication of sensors based on 3D graphene aerogels was achieved in two steps, in that the materials' synthesis was followed by the deposition step.<sup>7a,b,9,10</sup> Current strategies involving drop-casting or coating a suspension with graphene aerogel powders onto the platform fail to control their deposition, leading to variable morphology, uncontrolled coverage,

loss of surface area from aggregation, and poor electrical contact with the sensing electrodes.<sup>8a,11</sup> Direct integration of 3D graphene-based aerogels on a chip represents a significant challenge that requires integration of the materials' preparation/synthesis step into the fabrication of sensor devices. These strategies for *in situ* growth greatly simplify and strengthen the integration of the sensing material with the microheater platform, maximizing sensing performance, avoiding also issues of nanomaterial aggregation and poor electrical contact that conventional methods of materials' integration face.<sup>12</sup>

Here we report on the fabrication of chemiresistive gas sensors through the localized on-chip assembly of 3D interconnected porous polypyrrole (PPy) coupled graphene/W<sub>18</sub>O<sub>49</sub> nanowire aerogels. This was achieved with the redox reaction between graphene oxide (GO) and pyrrole (Py), which resulted in reduction of GO and polymerization of Py spontaneously without the addition of any other oxidizing or reducing agents. To further enhance the sensitivity of aerogel sensors to oxidizing gases such as NO<sub>2</sub>, W<sub>18</sub>O<sub>49</sub> nanowires were integrated into reduced graphene oxide (rGO) aerogels during the assembly process. As demonstrated previously, W<sub>18</sub>O<sub>49</sub> nanowires possess good sensing response to low concentrations of NO<sub>2</sub>.<sup>13</sup> These graphene based ternary aerogels facilitate gas adsorption by functioning as active gas adsorption sites, resulting in enhanced gas sensitivity, indicating their high potential for gas sensors. As a proof of concept, high-performance gas sensors based on graphene aerogels were fabricated and studied.

W<sub>18</sub>O<sub>49</sub> nanowires are synthesized *via* a mild solvothermal method. Fig. 1a shows the XRD pattern of the as-prepared W<sub>18</sub>O<sub>49</sub> nanowires. The narrow (010) and (020) reflections indicate that the crystal growth direction of W<sub>18</sub>O<sub>49</sub> nanowires is [010].<sup>14</sup> The high-resolution W4f spectrum can be deconvoluted into two doublets, which correspond to W<sup>6+</sup> and W<sup>5+</sup> oxidation states (Fig. 1b). The dominant peaks at 530.7 eV, 531.5 eV and 533.2 eV in the O 1s XPS spectra (Fig. 1c) represent the oxygen bond of W–O–W, oxygen vacancies and the adsorbed oxygen species,<sup>15</sup> respectively.

Fachgebiet Keramische Werkstoffe/Chair of Advanced Ceramic Materials,  
Technische Universität Berlin, Hardenbergstr. 40, 10623, Berlin, Germany.  
E-mail: [Gaofeng.shao@ceramics.tu-berlin.de](mailto:Gaofeng.shao@ceramics.tu-berlin.de), [gfshtao@nust.edu.cn](mailto:gfshtao@nust.edu.cn)

† Electronic supplementary information (ESI) available. See DOI: 10.1039/c9cc09092d



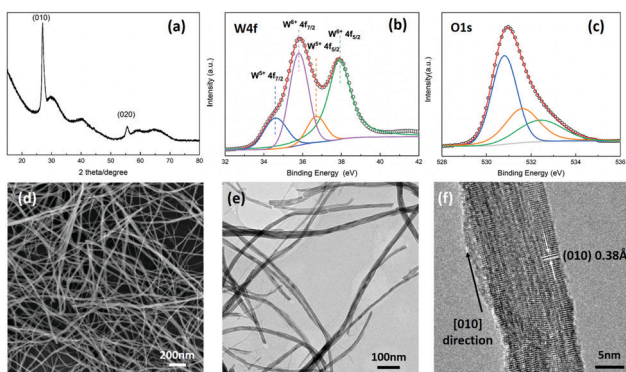


Fig. 1 (a) XRD pattern of  $\text{W}_{18}\text{O}_{49}$  nanowires, (b and c)  $\text{W}4\text{f}$  and  $\text{O}1\text{s}$  XPS spectra, (d) SEM and (e) TEM images of  $\text{W}_{18}\text{O}_{49}$  nanowires, and (f) HRTEM image of a single  $\text{W}_{18}\text{O}_{49}$  nanowire.

As shown in Fig. 1d and e, the as-grown  $\text{W}_{18}\text{O}_{49}$  is comprised of entangled nanowires with an average length of several micrometers and width of 10–20 nm. The wires are single-crystalline in nature, confirmed by HRTEM (Fig. 1f). Clear lattice fringes with a *d*-spacing of 0.38 nm can be discerned, corresponding to the (010) planes of monoclinic  $\text{W}_{18}\text{O}_{49}$ .<sup>16</sup> This implies preferential growth in the [010] direction, consistent with XRD observations.

Fig. 2 illustrates an *in situ* fabrication process of PPy coupled graphene/ $\text{W}_{18}\text{O}_{49}$  nanowire aerogels (PGWAs) on a chip (a  $\text{Al}_2\text{O}_3$  substrate integrated with a Pt electrode on the positive side and a Pt heater on the negative side). First, the substrate was hydroxyl functionalized by Piranha solution in order to increase the bonding strength between GO based solution and the substrate with hydrogen bonding. GO aqueous suspension and pre-synthesized  $\text{W}_{18}\text{O}_{49}$  nanowires were mixed together by ultrasonication, and then a reducing agent, a conductive polymer monomer, Py, was introduced (Fig. S2, ESI<sup>†</sup>). After that,  $\text{W}_{18}\text{O}_{49}$  nanowire containing Py/GO suspension was dropped on the chip by a syringe with a fine needle, followed by a polymerization-reduction process to functionalize it and initiate sheet assembly into a 3D network. After freeze-drying, the solvent was removed from the hydrogel to produce polypyrrole coupled reduced graphene oxide/ $\text{W}_{18}\text{O}_{49}$  nanowire aerogels (PrGOWAs). After the further annealing process, PGWAs were successfully integrated on a chip.

The direct on chip deposition is explained as follows. The GO sheet is hydrophilic mainly due to the ionizable  $-\text{COOH}$  groups at edges, while its basal plane is essentially hydrophobic due to a network of polyaromatic islands of unoxidized benzene rings.

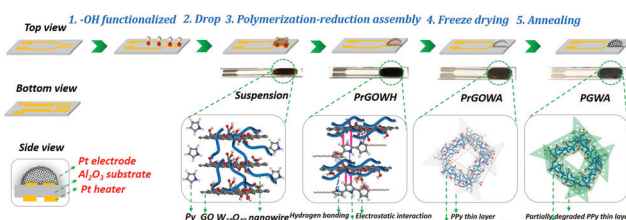


Fig. 2 Schematic illustration of the *in situ* fabrication process of 3D graphene based aerogels on a chip.

Therefore, the GO sheet can be considered as a surfactant with a largely hydrophobic basal plane and hydrophilic edge, and as a result, it would have the capability to disperse other nanomaterials in water homogeneously.<sup>17</sup> In this case, the GO sheets support and prevent insoluble  $\text{W}_{18}\text{O}_{49}$  nanowires from precipitation, forming stable suspensions. The Py monomer has a typical conjugated structure with an electron-rich N atom, which may easily attach on the surfaces and galleries of GO sheets through hydrogen bonding,  $\pi$ - $\pi$  stacking and electrostatic interaction,<sup>18</sup> coupling  $\text{W}_{18}\text{O}_{49}$  nanowires on graphene sheets simultaneously. Therefore, the existence of Py will effectively prevent the self-stacked behavior of GO during the reducing process, and accordingly increase the available GO sheets for forming a large volume of 3D graphene aerogels. A further annealing process was utilized for further reduction of GO and partial degradation of PPy, improving electrical contact and providing more chemisorption sites to enhance the response.

Fig. 3(a–d) show the SEM images of the PGWA on the  $\text{Al}_2\text{O}_3$  substrate interdigitated Pt electrodes. They present the features of tight adhesion between the PGWA and the device (Fig. 3(a)) and a highly porous structure with interconnected pores ranging from tens to hundreds of micrometers (Fig. 3(b)), which endows the sensing materials with low electrical resistance (Fig. S3, ESI<sup>†</sup>) and a high specific surface area of  $396 \text{ m}^2 \text{ g}^{-1}$  (Fig. S4, ESI<sup>†</sup>). In contrast to the smooth surface of graphene sheets, the  $\text{W}_{18}\text{O}_{49}$  nanowires are randomly decorated on the micrometer sized graphene sheet walls of the network (Fig. 3(c–e)), which are coupled by a PPy thin layer in the PGWA. Furthermore, the structure could be vividly described as a leaf tissue-like structure: PPy is the epi-dermis,  $\text{W}_{18}\text{O}_{49}$  nanowires are the leaf veins and graphene sheets are the mesophyll. For bare N-doped graphene aerogels, even when the annealing temperature reaches  $900^\circ\text{C}$ , the aerogels still show robust adhesion on the device with typical 3D interconnected porous structures (Fig. S5, ESI<sup>†</sup>). It is evident that this method is suitable for *in situ* assembly heteroatom-doped/defective graphene aerogels and nanomaterial functionalized graphene aerogels, which need post-treatment processes, such as high temperature annealing or plasma treatment.

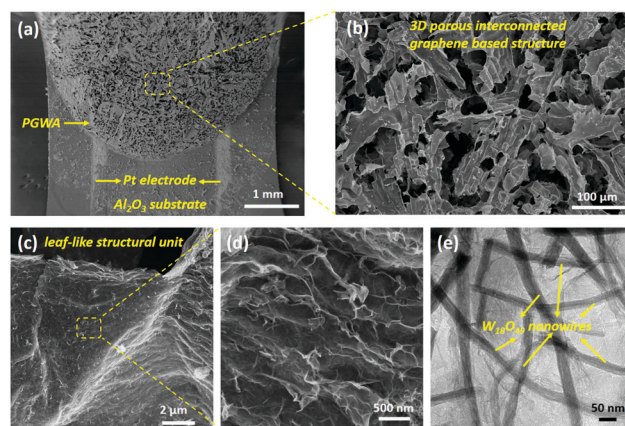


Fig. 3 (a–d) SEM images of the PGWA on a chip at different magnifications and (e) TEM image of the PGWA.

To confirm the interaction between PPy and graphene after the polymerization-reduction process, the ATR-FTIR spectra of GO and graphene based aerogels are shown in Fig. S6 and S7 (ESI<sup>†</sup>). It can be found that the bonds related to the C=O, C-OH and C-O groups of GO almost disappear, indicating the efficient reduction of GO. The strong band around  $1564\text{ cm}^{-1}$  is attributed to typical ring vibrations of PPy,<sup>19</sup> and that at  $1196\text{ cm}^{-1}$  is due to the C-N stretching.<sup>20</sup> The band at  $1041\text{ cm}^{-1}$  corresponds to the C-H band in plane vibrations, suggesting that PPy was indeed loaded onto the surface of graphene through interactions such as hydrogen bonding and  $\pi$ - $\pi$  stacking between them.<sup>19,21</sup> After the introduction of  $\text{W}_{18}\text{O}_{49}$  nanowires, peaks at  $787$  and  $715\text{ cm}^{-1}$  are observed, which are assigned to O-W-O stretching modes. The bands centered at  $655$  and  $585\text{ cm}^{-1}$  are attributed to the W-O-W stretching modes.<sup>22</sup> The partial characteristic peaks assigned to C-H in-plane and out-of-plane vibrations at  $1041\text{ cm}^{-1}$  and  $916\text{ cm}^{-1}$  of the PPy diminished after the annealing treatment, and no new characteristic peaks were observed, showing the degradation of the polymer. Furthermore, the chemical states of PGWAs are investigated by XPS (Fig. S8, ESI<sup>†</sup>). The initial GO is well reduced to graphene by polymerization-reduction and annealing processes, confirmed by significantly improving the intensity of  $\text{sp}^2$  C-C bonds of graphene at  $284.6\text{ eV}$  and decreasing the oxygen containing carbon (epoxy C-O at  $286.6\text{ eV}$ , carbonyl C=O at  $287.6\text{ eV}$ , and carboxyl O-C=O at  $288.9\text{ eV}$ ), as analyzed from the corresponding deconvolution of the C1s spectra of the as-prepared aerogels and GO (Fig. S9 and S10, ESI<sup>†</sup>). It should be noticed that the PGWA exhibits a nitrogen content of 4.26 at% after annealing (Table S1, ESI<sup>†</sup>). Besides, the high resolution N1s spectrum of the PGWA could be fitted well with three different signals corresponding to pyridinic N, pyrrolic N, and graphitic N, respectively (Fig. S11, ESI<sup>†</sup>), which further confirms PPy functionalization on the surfaces of graphene and N atoms doped in graphene. Further investigation of the phase evolution of GO is characterized by XRD. As shown in Fig. S12(a) (ESI<sup>†</sup>), the (001) crystal plane of GO was evident, with an interlayer spacing of  $8.33\text{ \AA}$ . After the polymerization-reduction process, the PGA showed a broad reflection at  $2\theta = 26^\circ$  (Fig. S12(b), ESI<sup>†</sup>), which is typical of reduced GO materials. The nanowires still exhibit the feature of a monoclinic crystal phase of  $\text{W}_{18}\text{O}_{49}$  after the further annealing process.

Based on all these findings, we can conclude that our fabrication procedure is suitable for the incorporation of 3D based graphene aerogels into electronic devices. As a proof-of-concept, the as-fabricated 3D graphene based aerogels are directly used as a gas sensor for the detection of low concentrations of  $\text{NO}_2$  gas. Fig. 4a shows the time dependent response of the graphene based aerogel sensors to various  $\text{NO}_2$  concentrations, from 200 to 975 ppb, with an operating temperature of  $140\text{ }^\circ\text{C}$  (Fig. S13, ESI<sup>†</sup>), which represents an optimum for the sensor signal and response/recovery time. At low temperature, the adsorption of  $\text{NO}_2$  is substantial and continues during gas exposure, while its desorption is negligible due to the strong bonding between  $\text{NO}_2$  and the PGA as well as the PGWA. The  $\text{NO}_2$  desorption is enhanced at higher temperature, which speeds up the time to reach a balance between adsorption and desorption both during

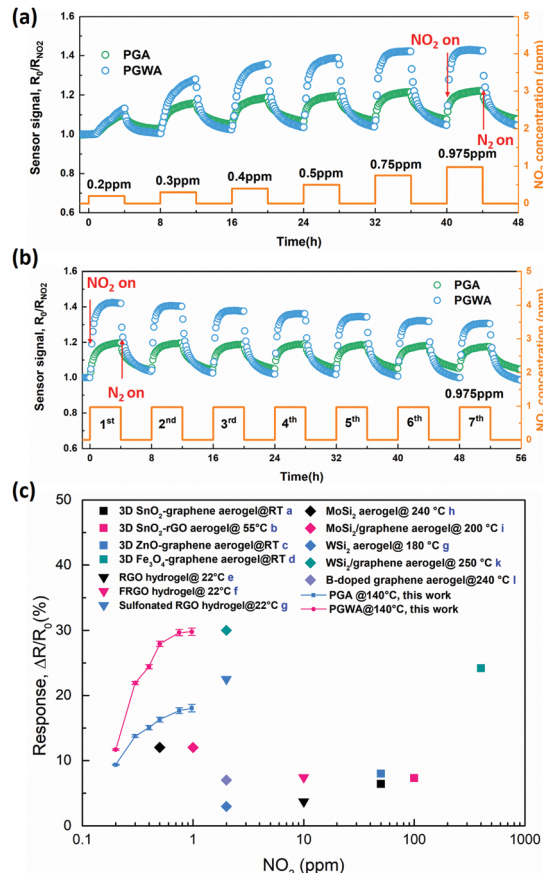


Fig. 4 (a) Transient sensor response at  $140\text{ }^\circ\text{C}$  towards different  $\text{NO}_2$  concentrations. (b) Reproducibility of sensor response exposed to  $0.975\text{ ppm}$   $\text{NO}_2$  at  $140\text{ }^\circ\text{C}$ . (c) Comparison with reported graphene based aerogels/hydrogels at optimized temperatures for  $\text{NO}_2$  sensors (a,<sup>24</sup> b,<sup>9</sup> c,<sup>25</sup> d,<sup>26</sup> e,<sup>11a</sup> f,<sup>8a</sup> g,<sup>7c</sup> h,<sup>27</sup> i,<sup>7b</sup> j,<sup>28</sup> k,<sup>10c</sup> l,<sup>10b</sup>).

gas exposure and during recovery. Although the response and recovery times might be even faster at higher temperature,  $140\text{ }^\circ\text{C}$  is considered an effective temperature when also considering the sensor signal.

Upon exposure to  $\text{NO}_2$  at  $140\text{ }^\circ\text{C}$ , the PGWA sensor presents higher response ( $\Delta R/R_0 = 29.78\%$ ) towards  $0.975\text{ ppm}$  of  $\text{NO}_2$  gas compared to the PGA sensor ( $\Delta R/R_0 = 18.04\%$ ) demonstrating the remarkably improved response achieved by functionalization with  $\text{W}_{18}\text{O}_{49}$  nanowires. Furthermore, to investigate the repeatability and stability of aerogel based sensors, the PGA and PGWA sensors were exposed to  $0.975\text{ ppm}$  of  $\text{NO}_2$  for seven successive cycles. An average response ( $\Delta R/R_0 = 25.4\%$ ) of the PGWA sensor with a small standard deviation of 1.9% is measured (Fig. 4b), verifying the reliable repeatability of the sensors. Moreover, compared with the gas sensing performance of graphene-based aerogels by the traditional deposition method (Fig. S14, ESI<sup>†</sup>), the PGWA assembled on a chip not only shows higher response, but also presents low noise of the sensor signal originating from its low electrical resistance (Fig. S15, ESI<sup>†</sup>).

Fig. 4(c) displays sensor response to  $\text{NO}_2$  above  $200\text{ ppb}$ , displaying a nonlinear relationship between the sensor response ( $\Delta R/R_0$ ) and gas concentration, which is typical for



chemiresistive sensors.<sup>23</sup> Assuming that the gas adsorption is dominated by high-energy defect sites, at low  $\text{NO}_2$  concentrations when most of the sites are available, the charge transfer is directly proportional to the gas concentration. At higher  $\text{NO}_2$  concentrations, all sites may eventually be occupied during the gas exposure, and thus the response reaches a saturation point.

To highlight the high sensing performance of the PGWA sensor fabricated in this work, the response of reported graphene based aerogels/hydrogels and two-dimensional metal sulfide aerogels are summarized in Fig. 4(c), which demonstrated the outstanding response towards low concentrations of  $\text{NO}_2$  gas.

The sensing performance of the *in situ* assembled 3D graphene based aerogels results from: (a) high conductivity of 3D interconnected graphene aerogels necessary for efficient operation of the sensors, (b) a highly porous structure with a high surface area that provides a large number of surface active sites necessary for the reliable detection of low  $\text{NO}_2$  concentrations, and (c) heterojunctions between n-type  $\text{W}_{18}\text{O}_{49}$  nanowires and p-type graphene as well as p-type PPy which is beneficial for enhancing gas sensitivity in chemiresistors.

In conclusion, we have successfully *in situ* assembled 3D interconnected porous PPy coupled graphene/ $\text{W}_{18}\text{O}_{49}$  nanowire aerogels on a chip by a polymerization–reduction route followed by an annealing process. Py initiates and mediates the assembly of GO sheets and  $\text{W}_{18}\text{O}_{49}$  nanowires into a 3D network in a facile, environment-friendly and scalable route. As a proof of concept, the as-fabricated 3D graphene based aerogels are applied as gas sensors for the detection of low concentrations of  $\text{NO}_2$  gas. The strategy developed here allows for direct integration of graphene based aerogels into functional devices and opens up new perspectives for the fabrication of functional devices.

## Conflicts of interest

There are no conflicts to declare.

## Notes and references

- 1 J. Mao, J. Iocozzia, J. Huang, K. Meng, Y. Lai and Z. Lin, *Energy Environ. Sci.*, 2018, **11**, 772–799.
- 2 N. Yousefi, X. Lu, M. Elimelech and N. Tufenkji, *Nat. Nanotechnol.*, 2019, **14**, 107–119.
- 3 B. Qiu, M. Xing and J. Zhang, *Chem. Soc. Rev.*, 2018, **47**, 2165–2216.
- 4 T. T. Tung, M. J. Nine, M. Krebsz, T. Pasinszki, C. J. Coghlhan, D. N. H. Tran and D. Losic, *Adv. Funct. Mater.*, 2017, **27**, 1702891.
- 5 S. S. Varghese, S. Lonkar, K. K. Singh, S. Swaminathan and A. Abdala, *Sens. Actuators, B*, 2015, **218**, 160–183.
- 6 Y. H. Zhang, Y. B. Chen, K. G. Zhou, C. H. Liu, J. Zeng, H. L. Zhang and Y. Peng, *Nanotechnology*, 2009, **20**.
- 7 (a) A. Harley-Trochimczyk, T. Pham, J. Chang, E. Chen, M. A. Worsley, A. Zettl, W. Mickelson and R. Maboudian, *Adv. Funct.*

*Mater.*, 2016, **26**, 433–439; (b) H. Long, A. Harley-Trochimczyk, T. Pham, Z. R. Tang, T. L. Shi, A. Zettl, C. Carraro, M. A. Worsley and R. Maboudian, *Adv. Funct. Mater.*, 2016, **26**, 5158–5165; (c) J. Wu, K. Tao, Y. Guo, Z. Li, X. Wang, Z. Luo, S. Feng, C. Du, D. Chen, J. Miao and L. K. Norford, *Adv. Sci.*, 2017, **4**, 1600319.

- 8 (a) J. Wu, K. Tao, J. Zhang, Y. Guo, J. Miao and L. K. Norford, *J. Mater. Chem. A*, 2016, **4**, 8130–8140; (b) T. Alizadeh and F. Ahmadian, *Anal. Chim. Acta*, 2015, **897**, 87–95.
- 9 L. Li, S. J. He, M. M. Liu, C. M. Zhang and W. Chen, *Anal. Chem.*, 2015, **87**, 1638–1645.
- 10 (a) D. M. Guo, P. J. Cai, J. Sun, W. N. He, X. H. Wu, T. Zhang, X. Wang and X. T. Zhang, *Carbon*, 2016, **99**, 571–578; (b) S. Turner, W. Yan, H. Long, A. J. Nelson, A. Baker, J. R. I. Lee, C. Carraro, M. A. Worsley, R. Maboudian and A. Zettl, *J. Phys. Chem. C*, 2018, **122**, 20358–20365; (c) W. Yan, M. A. Worsley, T. Pham, A. Zettl, C. Carraro and R. Maboudian, *Appl. Surf. Sci.*, 2018, **450**, 372–379.
- 11 (a) J. Wu, K. Tao, J. Miao and L. K. Norford, *ACS Appl. Mater. Interfaces*, 2015, **7**, 27502–27510; (b) N. H. Ha, D. D. Thinh, N. T. Huong, N. H. Phuong, P. D. Thach and H. S. Hong, *Appl. Surf. Sci.*, 2018, **434**, 1048–1054.
- 12 (a) M. Graf, A. Gurlo, N. Bârsan, U. Weimar and A. Hierlemann, *J. Nanopart. Res.*, 2006, **8**, 823–839; (b) L. Mädler, A. Roessler, S. E. Pratsinis, T. Sahm, A. Gurlo, N. Barsan and U. Weimar, *Sens. Actuators, B*, 2006, **114**, 283–295.
- 13 J. Polleux, A. Gurlo, N. Barsan, U. Weimar, M. Antonietti and M. Niederberger, *Angew. Chem.*, 2006, **118**, 267–271.
- 14 (a) G. Xi, S. Ouyang, P. Li, J. Ye, Q. Ma, N. Su, H. Bai and C. Wang, *Angew. Chem., Int. Ed.*, 2012, **51**, 2395–2399; (b) W. Cheng, Y. Ju, P. Payamyar, D. Primc, J. Rao, C. Willa, D. Koziej and M. Niederberger, *Angew. Chem., Int. Ed.*, 2015, **54**, 340–344.
- 15 X. Zhong, Y. Sun, X. Chen, G. Zhuang, X. Li and J.-G. Wang, *Adv. Funct. Mater.*, 2016, **26**, 5778–5786.
- 16 Y. Tian, S. Cong, W. Su, H. Chen, Q. Li, F. Geng and Z. Zhao, *Nano Lett.*, 2014, **14**, 2150–2156.
- 17 (a) Z. Niu, L. Liu, L. Zhang, Q. Shao, W. Zhou, X. Chen and S. Xie, *Adv. Mater.*, 2014, **26**, 3681–3687; (b) S. Hu, T. Han, C. Lin, W. Xiang, Y. Zhao, P. Gao, F. Du, X. Li and Y. Sun, *Adv. Funct. Mater.*, 2017, **27**, 1700041.
- 18 Y. Zhao, J. Liu, Y. Hu, H. Cheng, C. Hu, C. Jiang, L. Jiang, A. Cao and L. Qu, *Adv. Mater.*, 2013, **25**, 591–595.
- 19 J. Sun, X. Shu, Y. Tian, Z. Tong, S. Bai, R. Luo, D. Li and C. C. Liu, *Sens. Actuators, B*, 2017, **241**, 658–664.
- 20 X. Chen, J. Chen, F. Meng, L. Shan, M. Jiang, X. Xu, J. Lu, Y. Wang and Z. Zhou, *Compos. Sci. Technol.*, 2016, **127**, 71–78.
- 21 Z. Fan, J. Zhu, X. Sun, Z. Cheng, Y. Liu and Y. Wang, *ACS Appl. Mater. Interfaces*, 2017, **9**, 21763–21772.
- 22 (a) Y. Qin, T. Zhang and Z. Cui, *Org. Electron.*, 2017, **48**, 254–261; (b) B. Bhuyan, B. Paul, S. S. Dhar and S. Vadivel, *Mater. Chem. Phys.*, 2017, **188**, 1–7.
- 23 A. Gurlo, *Nanoscale*, 2011, **3**, 154–165.
- 24 X. Liu, J. S. Cui, J. B. Sun and X. T. Zhang, *RSC Adv.*, 2014, **4**, 22601–22605.
- 25 X. Liu, J. B. Sun and X. T. Zhang, *Sens. Actuators, B*, 2015, **211**, 220–226.
- 26 X. Liu, J. W. Li, J. B. Sun and X. T. Zhang, *RSC Adv.*, 2015, **5**, 73699–73704.
- 27 H. Long, L. Chan, A. Harley-Trochimczyk, L. E. Luna, Z. Tang, T. Shi, A. Zettl, C. Carraro, M. A. Worsley and R. Maboudian, *Adv. Mater. Interfaces*, 2017, **4**, 1700217.
- 28 W. Yan, A. Harley-Trochimczyk, H. Long, L. Chen, T. Pham, M. Hu, Y. Qin, A. Zettl, C. Carraro, M. A. Worsley and R. Maboudian, *FlatChem*, 2017, **5**, 1–8.

